Australian Meteorological and Oceanographic Journal 63 (2013) 377–389

Trapped mountain waves during a light aircraft accident

Teresa J. Parker[1] and Todd P. Lane[2]
[1]Monash Weather and Climate, School of Mathematical Sciences, Monash University
[2]School of Earth Sciences, The University of Melbourne

(Manuscript received November 2012; revised June 2013)

On 31 July 2007 a fatal light aircraft crash occurred near Clonbinane, Victoria, Australia and the official investigation concluded that mountain wave turbulence was the likely cause. This study uses three-dimensional numerical modelling and linear wave theory to examine the dynamics of mountain waves during this turbulence event and their role in generating turbulence. Analysis of the observed environment and three-dimensional idealised simulations elucidate the occurrence of trapped mountain waves and their role in creating regions of enhanced turbulence in the vicinity of the aircraft accident. Specifically, these waves perturb layers of low dynamic stability in the upstream flow, promoting turbulence in those layers. A simple ensemble of these three-dimensional simulations is also used to assess the robustness of the model solutions and demonstrate the utility of high-resolution ensembles for explicit mountain wave turbulence prediction.

Introduction

Turbulence is responsible for numerous injuries to passengers and crew on commercial airline flights every year and also poses a severe risk to light aircraft. While fatalities are rare in the commercial sector, they are more common in the general aviation sector. For example, in the United States turbulence contributes to tens of general aviation fatalities per year. Moreover, in recent years turbulence has also been the likely cause of several fatal accidents in the mountainous regions of Australia. This study examines the atmospheric processes and dynamics coinciding with a fatal light aircraft accident near Melbourne, Australia, specifically focusing on the role of mountain waves in generating turbulence.

A study of reported turbulence encounters involving commercial aircraft over the contiguous United States by Wolff and Sharman (2008) concluded that regions of complex terrain, such as the Rocky Mountains, constitute preferred locations of turbulence occurrence. Mountain waves, in particular, are commonly attributed as the cause of turbulence above mountains, especially at the cruise altitude of most commercial aircraft. In addition to mountain waves, other lower altitude terrain-induced phenomena contribute to the turbulence hazard for the general aviation sector as well as posing a danger to commercial aircraft during take-off and landing.

Corresponding author address: Tess Parker, School of Mathematical Sciences, Monash University, Australia. Email: Tess.Parker@monash.edu

Mountain waves, whether they are vertically propagating or trapped, are often too long in scale to influence aircraft directly. For example, horizontal scales of motion between approximately 50–1000 m will induce a turbulence response from large commercial aircraft (Lane et al. 2003); scales of motion that affect light aircraft are even shorter. Thus, some kind of instability or additional process is required to induce a cascade from the relatively long wave scale, down to sub-kilometre scales. Examples of these processes include trapped lee waves and rotors (Doyle and Durran 2002), wave breaking (Lilly 1978, Jiang and Doyle 2004, Lane et al. 2009), eddy shedding associated with mechanical effects (Clark et al. 1997), and shear instabilities that form within wakes (Lane et al. 2006). See Sharman et al. (2012) for a brief review.

Traditional approaches for operational turbulence avoidance and prediction employ empirical formulae or 'rules of thumb' designed to identify conditions conducive to mountain waves or mechanical effects. Disadvantages of these methods include limited intensity information and the spatial over-prediction of turbulence, which places considerable limits on available airspace. In the past, numerical weather prediction (NWP) offered little additional information because the coarse horizontal grid spacings (>~20 km) could not properly resolve mountain-scale flows and the hydrostatic assumption neglected many of the important nonhydrostatic processes (e.g. wave trapping). Yet modern high-resolution NWP models, with their nonhydrostatic formulations and grid spacings less than 10 km, offer much hope for future turbulence prediction

(e.g. Sharman et al. 2004). Other new approaches that employ satellite imagery for turbulence detection (e.g. Uhlenbrock et al. 2007) also represent an important development. Moreover, while the most significant recent advances in turbulence prediction for the aviation sector have focused on upper-level turbulence (e.g. Sharman et al. 2006), high-resolution NWP should provide substantial value at lower altitudes as well.

Even as horizontal grid spacings approach 1 km, numerical models are still unable to properly resolve the turbulence that influences aircraft. Nevertheless, these models still contain valuable information about the turbulence-causing instabilities, such as wave dissipation, at the smallest resolvable scales or through parameterised sub-grid scale processes. Moreover, as shown by Lane et al. (2009), turbulence is often linked to larger scale flow patterns that are well resolved and predictable, and parameterised turbulence can provide a good representation of turbulence locations. More sophisticated post-processing of NWP model output using spectral downscaling methods (e.g. Frehlich and Sharman 2004) is also an option. Arguably, explicit turbulence predictions should be more successful for turbulence near terrain than some other turbulence sources (e.g. moist convection; see Lane et al. 2012) because the source of the turbulence (viz. the mountains) remains fixed and the predictability limits should be less restrictive.

This study is motivated by a light aircraft crash in mountainous terrain, which occurred on the northern outskirts of Melbourne, Victoria, Australia. Shortly after 1000 UTC (2000 local time) 31 July 2007, a Rockwell Commander light aircraft traveling approximately north-northeast from one of Melbourne's smaller airports, Essendon Airport (airport code: MEB, automated weather station code: MEN; see Fig. 1(b)), crashed near Clonbinane, Victoria, killing both the pilot and passenger. Radar and radio contact was lost approximately 46 km north-northeast of Essendon and 2.1 km above mean sea level (AMSL). The wreckage was spread over a wide area in timbered hilly terrain at an elevation of about 425 m and its location is also shown in Fig. 1(b). As part of the official investigation by the Australian Transport Safety Bureau (ATSB 2009), examination of the wreckage revealed levels of mechanical deformation in the main wing spar elements consistent with failure and separation of both outer wing sections under downward bending loads. This analysis along with the spatial distribution of the aircraft wreckage provided clear evidence of aircraft breakup during flight. The ATSB investigation concluded that the breakup 'most likely resulted from an encounter with localised and intense turbulence, or from an elevator control input, or from a combination of both'. The investigation also cited the potential role of mountain wave turbulence in contributing to the incident.

As shown by the 0600 UTC 31 July 2007 mean sea level pressure analysis (Fig. 2), the flow over the southeast Australian area was characterised by an approaching cold front that was predicted to pass through Melbourne early

Fig. 1. Terrain elevation: (a) shows a region of southeast Australia and the black box denotes the location of the inset map shown in (b). Shading is at intervals of 0, 250, 500, 750 and 1000 m above mean sea level, with these levels also contoured in (b). The blue box denotes the large model domain, and the red box the size and location of the smaller domain that is used for sensitivity studies. (b) Observed 10 m winds at 1200 UTC 31 July 2007 from the Bureau of Meteorology METARS (blue wind barbs) for airport observations at Bendigo (BDG), Ballarat (BLT), Mt Hotham (HOT), Essendon (MEN), Melbourne (MML), Mangalore (MNG), and Shepparton (SHT). The position of the aircraft wreckage is denoted W. Also shown in red are 10 m winds from the control simulation. Standard meteorological convention is used for the barbs: long barbs are 10 knots and short barbs are 5 knots.

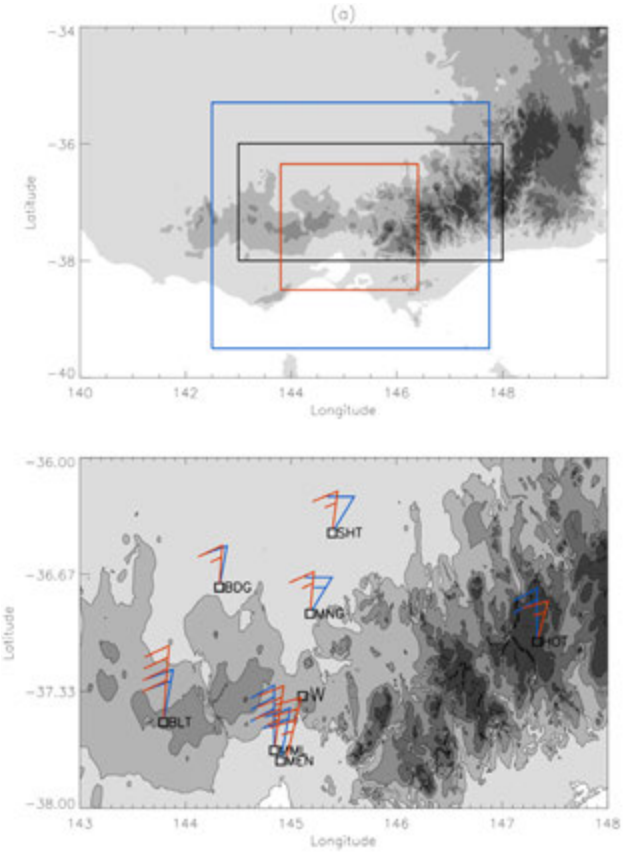

the following morning. The pre-frontal air was predicted to contain strong gusty north to northwesterly winds of up to 20 m s^{-1} to an altitude of 3 km. The Australian Bureau of Meteorology issues regular aviation forecasts and SIGMETs (significant meteorological event advisories), which provide warnings to the aviation sector of potentially hazardous weather conditions. Two SIGMETs issued on the day of the accident warned of severe (mechanical) turbulence up to 2.4 km altitude, near and to the south of the mountain ranges, and occasional severe mountain wave turbulence between 1.5 and 4.3 km altitude. Flights arriving in or departing from the Melbourne area around the time of the accident reported strong wind speeds but no significant turbulence; however, a fixed-wing search aircraft reported significant, continuous

turbulence between 1.5 and 1.9 km above the wreckage area during the search, and turbulence encounters were reported by pilots approaching Melbourne in the three hours subsequent to the accident (ATSB 2009).

The aim of this study is to examine the dynamics and characteristics of the mountain waves that occurred on 31 July 2007, and to determine what role, if any, these waves had in causing turbulence during the event. The remainder of the paper describes the observed environment; the numerical model, the characteristics of simulated mountain waves, analysis of the environment using linear theory, the influence of the waves on parameterised turbulence, and the sensitivity of the results to model resolution and wind direction; and finally, a summary of the results.

Fig. 2. Mean sea level pressure analysis valid 0600 UTC 31 July 2007 (courtesy Bureau of Meteorology).

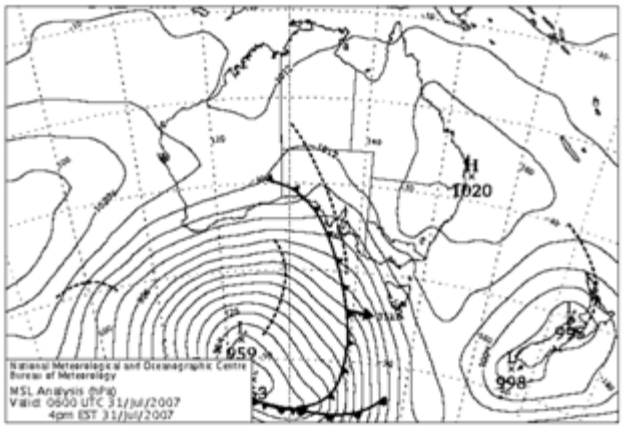

Characteristics of the observed environment

The accident occurred approximately 50 km to the north-northeast of the release-point of the routine Melbourne sounding, only two hours before the 1200 UTC 31 July 2007 launch (the Melbourne sounding is released approximately 8 km to the northwest of MEN). This sounding therefore provides a good representation of the atmospheric conditions at the time of the accident, albeit downstream of the terrain. The 1200 UTC 31 July 2007 Melbourne sounding (hereafter referred to as simply the Melbourne sounding) is shown in Fig. 3.

The Melbourne sounding features strong surface winds that exceed 15 m s^{-1}, then increase in magnitude to reach 28 m s^{-1} by 1 km altitude (Fig. 3(a)). Beyond this local maximum, the wind speed generally increases until it reaches 60 m s^{-1} at about 11 km and then decreases further aloft. The wind direction remains in the northwest quadrant for almost the entire sounding (Fig. 3(b)), but varies considerably over the lowest 3 km: it is 350° near the surface and 280° at approximately 4.5 km. The tropopause is at approximately 10 km (Fig. 3(c)), which is just below the 60 m s^{-1} jet. Near the surface the sounding is stable (recall this is a nocturnal sounding), with a strong inversion identified by a rapid increase in potential temperature at 1 km. Beyond this inversion the troposphere continues to be stable, except there is a layer of reduced stability between approximately 3 and 4 km.

The height of the terrain (h) in the vicinity of the aircraft accident peaks at approximately 200 m above the surrounding orography, the Brunt-Väisälä frequency (N) in

Fig. 3. Profiles of (a) wind speed, (b) wind direction, and (c) potential temperature from the 1200 UTC 31 July 2007 Melbourne sounding.

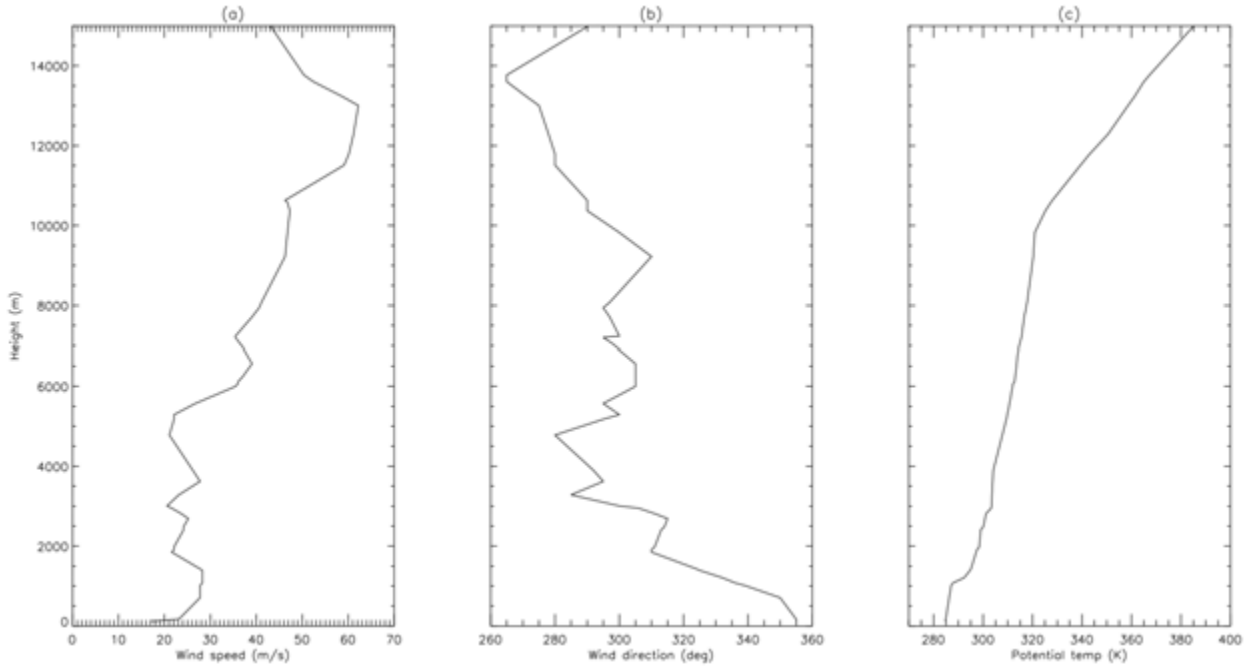

the lowest 1 km of the atmosphere is approximately 0.01 s^{-1}, and the wind speed below terrain height (u) is approximately 20 m s^{-1}. Therefore, the nondimensional mountain height, Nh/u, is 0.1, which is small and suggests a linear flow regime and relatively little flow blocking with conditions conducive to mountain wave generation (see e.g. Smolarkiewicz and Rotunno 1989). The strong speed and directional shear in the lower troposphere, accompanied by the substantial vertical variations in stability, suggest that significant changes in vertical propagation characteristics could occur in this environment leading to wave evanescence, trapping, or some kind of wave dissipation. However, the rotation of the near-surface winds and the complexity of the terrain make it difficult to identify the likely direction of the dominant wave vector, which will be examined in the next section in the context of the numerical modelling results.

Automated weather station observations across Victoria of the 10 m wind at 1200 UTC 31 July 2007 illustrate some of the spatial variability of the wind speed and direction (Fig. 1(b)). In the lee of the terrain there is significant enhancement in the wind speed. At Melbourne (MML) and Essendon (MEN) airports the observed wind speeds of 20–30 knots are notably larger than those upwind of the terrain (e.g. Shepparton [SHT], Bendigo [BDG], and Mangalore [MNG]). This wind speed enhancement and the northerly direction at both MML and MEN imply that the wind is flowing over the terrain. The wind direction at SHT and MNG has a ridge-parallel component, which is suggestive of partial blocking of the flow. Thus, the enhanced lee-side flow might be related to classical 'downslope' flow (e.g. Durran 1986) or partial blocking and funnelling of the flow through the terrain north of MML. Finally, the different wind directions at MML and MEN indicate local convergence.

The numerical model

In this section a three-dimensional model is used to examine aspects of the terrain-induced flows during the event.

(a) Model description

The numerical model was originally developed by Clark (1977) and has been used to study a variety of terrain-induced flows, including low-level turbulence in the lee of Lantau Island (Clark et al. 1997), mountain wakes (Lane et al. 2006), clear air turbulence during a downslope windstorm (Clark et al. 2000), and mountain waves over the New Zealand Southern Alps (Lane et al. 2000). It is a finite-difference approximation to the non-hydrostatic and anelastic equations of motion featuring a terrain-following vertical coordinate and a first order sub-grid scale mixing parameterisation (Smagorinsky 1963, Lilly 1962). See Clark et al. (1996) for further details of the model formulation. The model is used in a quasi-idealised configuration, designed to examine the susceptibility of the environment to mountain waves. Among other things, such a configuration allows simple changes to be made to the simulated environment, which can isolate the underlying dynamics.

Two different size model domains are used: the larger domain is approximately 474 km on each lateral boundary and the smaller domain is approximately 237 km on each lateral boundary. These domains are hereafter referred to as the large domain and small domain, respectively, and are both centred on the wreckage site as illustrated in Fig. 1(a). The model topography is derived from a 30 arcsecond resolution dataset obtained from the National Geophysical Data Center / National Oceanic and Atmospheric Administration. At the latitude of the aircraft wreckage, approximately 37.4°S, the topography data have a resolution of approximately 740 m in the zonal and 925 m in the meridional directions. For use in the model, these data are interpolated onto a square Cartesian grid and the topography averaged to remove features with scales equal to two times the horizontal grid spacing. Horizontal grid spacing of either 1.85 km or 0.925 km is used depending on the simulation. The vertical grid has 128 points; near the surface, the vertical grid spacing increases from 25 m until it reaches 200 m at approximately 500 m altitude, above which the spacing is constant. The model extends to 25 km, with an absorbing layer in the uppermost 10 km to mitigate reflections from the upper boundary.

The model is initialised with horizontally uniform initial conditions and integrated with open boundary conditions. The time step is five seconds and the simulations are conducted for six hours when they are approximately at steady state; the six-hour model results are examined throughout the remainder of this paper. Although not shown here, other times near the end of the simulation were examined, but the results were extremely similar to the six-hour results. The effects of the earth's rotation are included via normal Coriolis terms. Surface friction is represented using a simple topography-dependent roughness length formula: for ocean grid points the roughness length is 0.5 mm, the roughness length increases linearly with terrain elevation to 0.5 m at 1000 m elevation, and is equal to 0.5 m at grid points with terrain higher than 1000 m. Clearly, this scheme is an oversimplification of the real surface roughness, except the roughness pattern compares reasonably well with more sophisticated models in the region of interest (not shown) and has formed the basis of a number of other studies (e.g. Clark et al. 2000, Lane et al. 2006). Since the aircraft accident occurred at night and there was no precipitation observed from the prefrontal air mass, moist processes and surface heating are neglected.

(b) Three-dimensional simulation results and the modified sounding

The first simulation to be considered uses the small domain with horizontal grid spacing of 1.85 km. This simulation is initialised with a horizontally uniform initial state defined by the Melbourne sounding. After six hours of simulation time, however, the vertical profile of the simulated wind at the location of the Melbourne sounding (dotted-dashed

Fig. 4. Profiles of horizontal wind speed. (a) The Melbourne sounding (dashed), the upstream profile from the MesoLAPS analysis (dotted-dashed), and the modified sounding (solid). (b) Simulated wind speed at the approximate location of Melbourne Airport (after six hours) for the small domain simulation initialised with the Melbourne sounding (dotted-dashed) and the control simulation initialised with the modified sounding (solid). Also shown in (b) for comparison purposes is the Melbourne sounding (dashed).

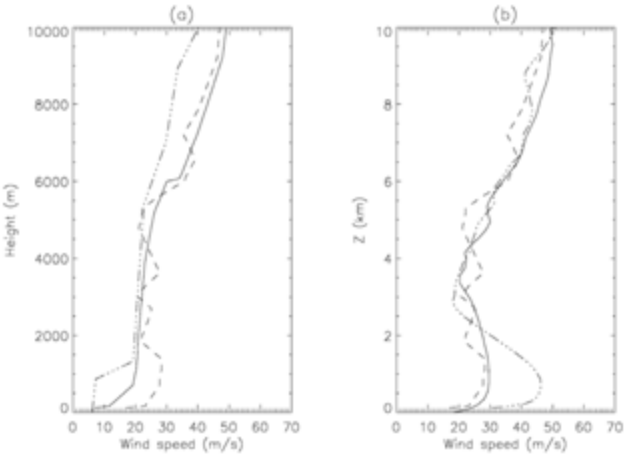

line in Fig. 4(b)) reveals that the low-level wind speeds are considerably stronger than the Melbourne sounding observations. Further inspection of the simulated fields (not shown) identifies enhancement of the low level winds in the lee of the terrain. Although enhancement of the low-level winds in the lee of the terrain is in general agreement with the observations shown in Fig. 1(b) and is a characteristic of the flow regime, the Melbourne sounding, with its downstream location, is unduly affected by the terrain-induced flows. The sounding does not provide the best representation of the upstream conditions and a wind profile more representative of the conditions upstream needs to be used.

Unfortunately, no radiosondes were released from upstream sounding locations (e.g. Wagga Wagga, New South Wales) at the appropriate time. Instead, data from the Bureau of Meteorology's MesoLAPS analysis (Puri et al. 1998) is used to guide modifications to the initial wind profile for the simulations. The upstream (145°E, 36.25°S) wind profile from the MesoLAPS analysis at 1200 UTC on 31 July 2007 is shown in Fig. 4(a) (dotted-dashed line). This upstream profile has significantly weaker surface winds than the (downstream) Melbourne sounding. With this in mind an ad hoc approach, which involved re-running the small domain simulation a number of times with systematically reduced upstream low-level wind speed, was used to determine modifications to the Melbourne sounding that provided the best agreement between the model and the Melbourne sounding at its release location; the resultant wind profile is shown in Fig. 4(a) (solid line) and it is hereafter referred to as the modified sounding. Note that the modified sounding is also subjected to some (minimal) smoothing before being used to initialise the model.

Fig. 5. Wind vectors at six hours from the control simulation from the lowest model level (12.5 m AGL). Grey contours indicate the coastline and topography contoured at 200 m contour intervals (starting at 100 m). The reference vector in the bottom right corner is 20 m s^{-1}.

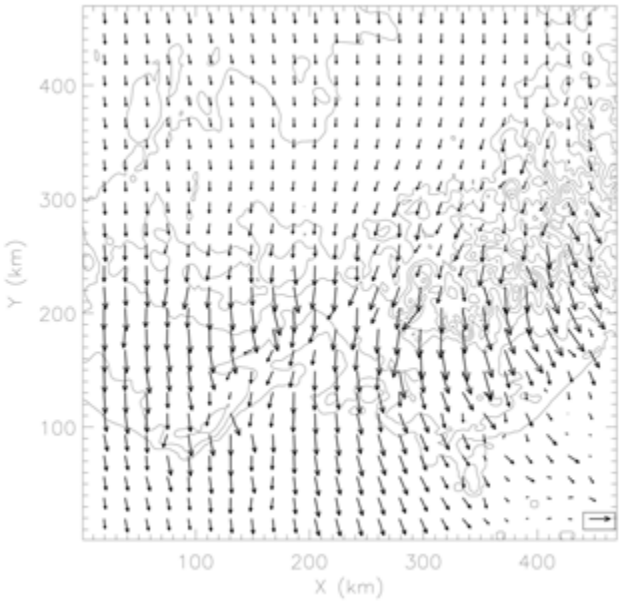

A simulation using the large domain with 1.85 km horizontal grid spacing is initialised with the modified sounding. This simulation is hereafter referred to as the control simulation. The simulated wind profile at the location of the Melbourne sounding is shown in Fig. 4(b) (solid line). This simulated wind profile shows good agreement with the Melbourne sounding (dashed line) and the profiles of potential temperature also compare well (not shown). Thus, while this approach of modifying the observed sounding is not ideal, it provides a realistic representation of the conditions downstream of the terrain. By using the observed sounding, important features in the vertical structure of the shear and stability profiles further aloft are maintained—many of these structures are not represented particularly well by the LAPS analysis. The vertical structure of the shear and stability is critical in defining the characteristics of the wave propagation.

Figure 5 shows the wind vectors from the control simulation at the lowest model level (12.5 m above ground level (AGL)) at six hours. In agreement with the observations (Fig. 1(b)), the model demonstrates cross-mountain flow that is stronger in the lee of the mountains. The wind has a northeasterly component around (x,y)=(300, 300) km, indicative of partial flow blocking. Moreover, in the vicinity of Melbourne and Essendon airports [(x,y)≈(220,200) km] the wind vectors indicate similar convergence to the observations (Fig. 1(b)).

The model winds, converted from those at the lowest model level to 10 m AGL using the logarithmic wind profile, are also overlaid on Fig. 1(b) allowing direct comparison to

the observations. Figure 1(b) demonstrates good agreement in the modelled wind at Melbourne and Essendon airports, except the modelled wind direction is approximately ten degrees east of the observations. The wind upstream of the terrain has approximately the correct speed; the modelled wind direction has good agreement at Bendigo, but at Shepparton and Mangalore the modelled direction is about 20 degrees north of the observations. This difference in direction suggests that blocking effects are slightly more prevalent in the observations than the model, and there is a bias in the upstream wind direction. Nonetheless, it will be shown later that the simulated flow characteristics are relatively insensitive to small variations in upstream wind direction and the differences in low-level wind direction are not a major concern.

A cross section of vertical velocity from the control simulation at six hours at approximately 1.9 km AGL (Fig. 6(a)) shows trapped lee waves extending a significant distance downstream of the terrain. The wave fronts feature a variety of orientations, but the predominant orientation is southwest to northeast. In the area of the aircraft accident (in the middle of the domain) trapped waves are also evident with wave fronts oriented southwest to northeast, which implies that the wave vector points approximately to the northwest.

The profiles of wind shear (magnitude and direction) calculated from the Melbourne sounding (not shown) show that above the strong shear layer at the surface, the magnitude of the wind shear is almost constant until 1.5 km; the direction of the shear vector at the surface points from the north, but rotates anticlockwise to point from the west at approximately 1 km. Hence, the mean low-level shear vector points from the northwest. Thus, as is common, the predominant wave vector orientation is aligned in approximately the opposite direction to the mean low-level shear vector.

A cross section of vertical velocity from the control simulation from the northwest to southeast and passing through the accident location (Fig. 6(b)) shows the vertical structure of the trapped waves. Some waves are trapped below approximately 4 km, with others extending throughout the troposphere. The amplitudes of the waves are maximised near 2 km altitude, exceeding 2 m s^{-1} (vertical velocity) at some locations, with the largest amplitudes directly adjacent to the location of the aircraft accident (marked with a cross). The horizontal wavelength varies between approximately 15 km at around 550 km distance and 25–30 km between about 300 and 500 km distance, and waves with longer wavelengths penetrate deeper while the shorter wavelength waves are trapped below 4 km. Those longer wavelength waves that extend above 4 km are vertically propagating (see for example around 400 km distance) because their phase lines are tilted towards the northwest with altitude. At the accident location (approximately 330 km distance) some evidence of sporadic or recently terminated vertical propagation is evident, suggesting that the horizontal wavelengths in this region may be close to the critical point.

As shown in Fig. 6, the complex terrain generates a rich spectrum of waves that contains a variety of horizontal scales and wave orientations. For example, in the vicinity of (x,y) = (400,180) km in Fig. 6(a), the lee waves show a complex interference pattern; wave fronts with south–north orientation occur alongside wave fronts with southwest–northeast orientations. These structures that are more closely aligned with the upstream flow appear similar to complex lee wave structures identified in other modelling studies (e.g. Lane et al. 2000), and may be related to large valleys on the lee side of the mountain ranges (e.g. Fig. 1(b)).

(c) Linear wave theory

The vertical variations in wave propagation characteristics are considered by analysing the Scorer parameter (Scorer 1949). Specifically, by employing linear theory the dispersion relation for a nonhydrostatic fluid can be written as

$$m^2 = l^2 - k^2 \qquad ...(1)$$

Fig. 6. Vertical velocity from the control simulation (coloured shading). (a) Horizontal cross section at approximately 1.9 km AGL; contours are at 0.5 m s^{-1} intervals, with negative values dashed and the zero contour omitted. Grey lines indicate the coastline and topography contoured at 200 m contour intervals (starting at 100 m). (b) Cross section from northwest (left) to southeast (right) through the centre of the domain, contoured at 0.5 m s^{-1} intervals: only the part of the domain showing wave features is included and the cross marks the accident location.

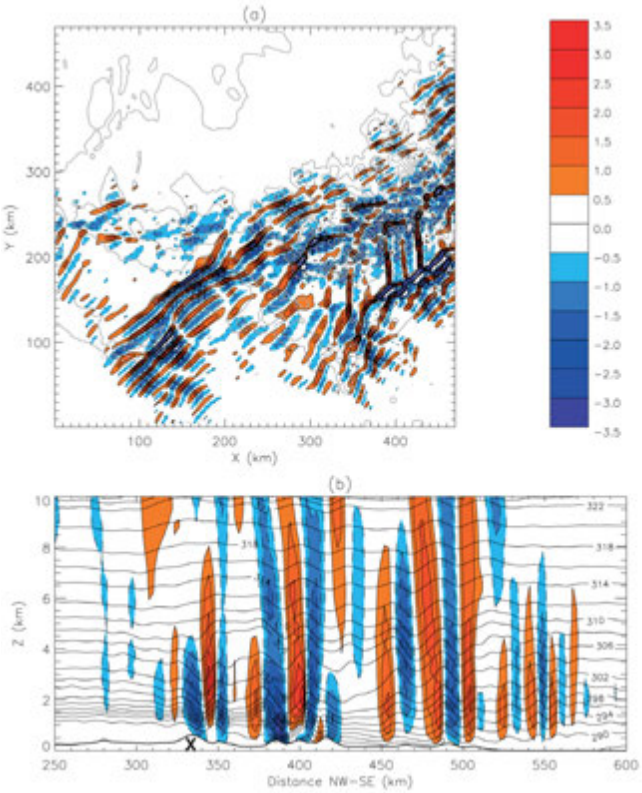

where m is the vertical wavenumber, k is the horizontal wave number, and l^2 is the Scorer parameter. Making the usual assumptions, viz. steady mountain waves and a density scale height that is infinitely large, the Scorer parameter can be written in simplified form as

$$l^2 = \frac{N^2}{U^2} - \frac{U_{zz}}{U} \qquad ...(2)$$

where $U(z)$ is the component of the background wind in the direction that opposes the horizontal orientation of the wave vector, and U_{zz} its second derivative in the vertical. It follows from (1) that m is a real number when $l^2 > k^2$ and therefore vertically propagating wave solutions exist. At heights where $k^2 > l^2$, m is complex-valued and the physical wave solutions are evanescent, i.e. the amplitude decays exponentially with height. The critical horizontal wavelength (λ_c), defined as

$$\lambda_c = \frac{2\pi}{l} \qquad ...(3)$$

delineates the transition from vertically propagating to evanescent solutions; wavelengths shorter than λ_c are evanescent. Layers of evanescence can lead to wave trapping, which is more prevalent for the shorter horizontal wavelengths that are usually generated by small-scale terrain features. Typically, wave trapping requires a layer near the surface where waves can propagate vertically (i.e. the horizontal wavelengths are greater than λ_c) with an evanescent layer (i.e. the horizontal wavelengths are less than λ_c) further aloft. This arrangement defines a resonant duct between the surface and the evanescent layer, trapping wave energy within this duct and allowing waves to extend downstream.

To calculate the Scorer parameter and critical horizontal wavelength the direction of the wave vector must be assumed to determine the appropriate wind profile to use. For two-dimensional flows or simple three-dimensional flows over simple terrain, this is relatively straightforward. Yet, the aircraft accident occurred over relatively complex terrain that features a variety of ridge orientations, and the environment contains significant directional shear at low levels. Therefore, the dominant wave vector direction cannot necessarily be determined a priori. Nevertheless, the previous section showed that in the control simulation the predominant wave vector direction near the accident site was directed towards the northwest and opposing the mean low-level shear vector. Thus, the 315° component of the wind is used here to determine the vertical profile of the critical horizontal wavelength.

Figure 7 shows the 315° component of the wind and the critical horizontal wavelength calculated using the modified sounding (thick lines) and the original Melbourne sounding (thin lines). These two profiles of critical wavelength are indicative of the environment upstream and downstream of the terrain. Despite the differences in the profiles of critical wavelength below 6 km (due to the differences in wind speed and wind curvature exposed in Fig. 7(a)), both

Fig. 7 (a) The 315° horizontal wind component and (b) critical horizontal wavelength calculated from the modified sounding (thick line) and the Melbourne sounding (thin line).

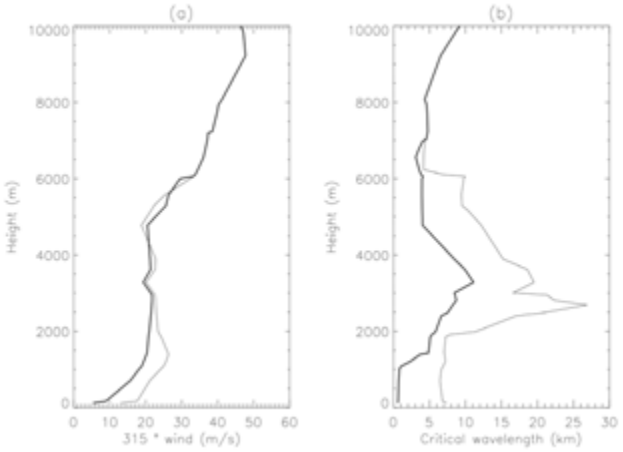

profiles of the critical wavelength show features consistent with the modelled waves in the control simulation. Both profiles highlight the possibility of trapping of waves with horizontal wavelength less than approximately 10–20 km below approximately 3 km. This altitude corresponds to the layers of reduced static stability between 2 km and 4 km identified in Fig. 3(c). Arguably, the Melbourne sounding provides a better representation of the environment the waves actually experienced and suggests trapping of waves with up to 25 km wavelength below 3 km, which is in good agreement with the control simulation. Moreover, both profiles suggest that longer wavelength (>25 km) mountain waves could propagate vertically and extend throughout the troposphere, which is also in agreement with Fig. 6(b).

Thus, the preceding analysis using linear theory and the control simulation have demonstrated that the environment observed on 1200 UTC 31 July 2007 was conducive to trapped lee waves. Indeed, available high-resolution satellite images at 0500 UTC 31 July and 0000 UTC 1 August also show some evidence of lee wave activity over Victoria (not shown). In the next section, the contribution of the simulated waves to turbulence production is considered.

(d) Enhanced turbulence due to trapped mountain waves

As shown in (b) above, in the 3D simulation the site of the aircraft accident is surrounded by widespread (sometimes trapped) mountain waves. Furthermore, the amplitude of those waves is large near the site of the accident. However, atmospheric gravity waves are not necessarily turbulent per se and their horizontal wavelengths are often too large to induce a turbulent aircraft response. Turbulence from mountain waves requires wave breaking or another instability to initiate a turbulent cascade. The role of the trapped gravity waves in creating regions of enhanced turbulence is considered in this section.

At the model resolutions considered herein, viz. ~2 km horizontal grid spacing and 200 m vertical grid spacing, turbulence is not properly resolved and must be parameterised. The Clark model parameterises sub-grid scale mixing using a first-order Smagorinsky-Lilly (Smagorinsky 1963, Lilly 1962) scheme. In its current configuration, the diagnosed eddy mixing coefficient of momentum, K_M, is non-zero where the Richardson number, *Ri*, is less than 1; the assumed eddy Prandtl number is 1. Thus, regions of the flow that contain dynamical (or thermodynamic) instability feature non-zero K_M, which is used to diagnose likely locations of turbulence or enhanced turbulence at unresolved scales. For the analysis considered here, the eddy mixing coefficient is converted to a more intuitive quantity, viz. sub-grid turbulence kinetic energy per unit mass (*TKE*), using Deardorff's (1980) formula, $TKE = (10K_M/l)^2$, where the length scale l is defined here as the vertical grid spacing.

A cross section at approximately 1.9 km AGL (Fig. 8) shows areas of *TKE* extending over the mountains, encompassing the location of the aircraft accident. These areas of *TKE* approximately coincide with the locations of the trapped lee waves (Fig. 6(a)). A vertical cross section of *Ri* and *TKE* from northwest to southeast and passing through the accident site (Fig. 9) demonstrates that the non-zero *TKE* at 2 km altitude near the aircraft accident originates from two processes. The first process is the descent of a dynamically unstable layer ($Ri < 1$) that is located at approximately 3 km in the upstream sounding. The upstream flow has a shallow layer with $Ri < 1$ at this altitude, which is due to a combination of a maximum in the wind shear (not shown) and reduced stability (Fig. 3(c)). Above the accident site this layer of low *Ri* descends by more than a kilometre with substantial enhancements in *TKE* (further reductions in *Ri*). Inspection of cross-sections of potential temperature, the 315° component of the wind and the vertical shear (Fig. 10) shows that these perturbations in *Ri* are indeed mountain-wave induced. The trapped waves cause large perturbations in wind shear and stability, which lead to perturbations in the *Ri*. In particular, directly above the accident site the potential temperature (Fig. 10(a)) identifies significant descent caused by the mountain waves between 2 km and 4 km. This descent is also collocated with large perturbations in the 315° wind component (Fig. 10(b)) that result in a strengthening of the shear above the accident site. The descent of the shear layer and reduction in stability both approximately coincide, indicating that these perturbations both contribute to the reduction in *Ri*.

Fig. 8. Horizontal cross section of subgrid turbulence kinetic energy per unit mass (*TKE*) at approximately 1.9 km AGL. The maximum value shown is approximately 1 $m^2 s^{-2}$. Topography contours are the same as Fig. 6(a).

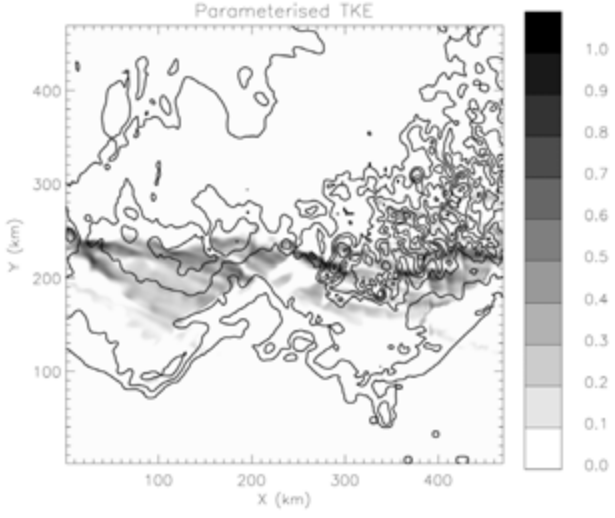

An ascending layer of enhanced *TKE* near the accident site is the second important process inducing *TKE* near 2 km altitude. While the upstream flow is statically stable near the surface (Fig. 3(c)), the very strong wind shear near the surface (not shown) causes the near-surface air to have low *Ri*. The resultant parameterised mixing also acts to further reduce the static stability. Over the mountains, mechanical effects cause this dynamically unstable layer to deepen. Moreover, near the accident site (distance = 350 km) and further downstream (distance = 400 km) the large amplitude lee waves cause ascent of the turbulent near-surface air (Fig. 9). The result is significantly enhanced *TKE* that extends from the surface to almost 2 km altitude in a few horizontal locations. This pattern is similar to that described by Doyle and Durran (2002), who showed how lee waves can cause the ascent of the surface layer vorticity sheet in the context of rotors. However, in this case the lack of reversed flow (cf. Fig. 10(b)) means no rotors are present here. This lack of rotors may properly reflect the underlying dynamics of the system or may be influenced by the model resolution. Figure 9 also shows some similarity to results of boundary layer separation in the lee of terrain described by Jiang et al. (2007).

In summary, the model simulations demonstrate substantial enhancements in the sub-grid *TKE* in the vicinity of the aircraft accident. The occurrence and enhancement of *TKE* is directly related to pre-existing regions of instability in the upstream flow, viz. the layer of low *Ri* near 2 km and low *Ri* near the surface, that are modified by trapped mountain waves.

(e) Sensitivity to domain size and resolution

In this section, the sensitivity of the simulated mountain waves to domain size and horizontal resolution is briefly considered. To examine the sensitivity to domain size, a simulation using the small domain with 1.85 km grid spacing is initialised with the modified sounding. A comparison of the vertical velocity at approximately 1.9 km AGL for the control simulation (Fig. 11(a)) and the small domain simulation (Fig. 11(b)) shows that there is some sensitivity to domain size, caused by the interaction of the flow with the open boundary conditions. In the southwest part of the figures the wave fronts in the small domain simulation are shorter and less coherent, whereas in the control simulation the wave fronts are longer and better defined. Nevertheless, near the aircraft

Fig. 9. Richardson number (Ri, contours) and TKE in m² s⁻² (shaded) along the cross section from the northwest (left) to southeast (right) through the centre of the domain. Ri is contoured at 0, 0.25, 1 and 10. A red cross marks the accident location.

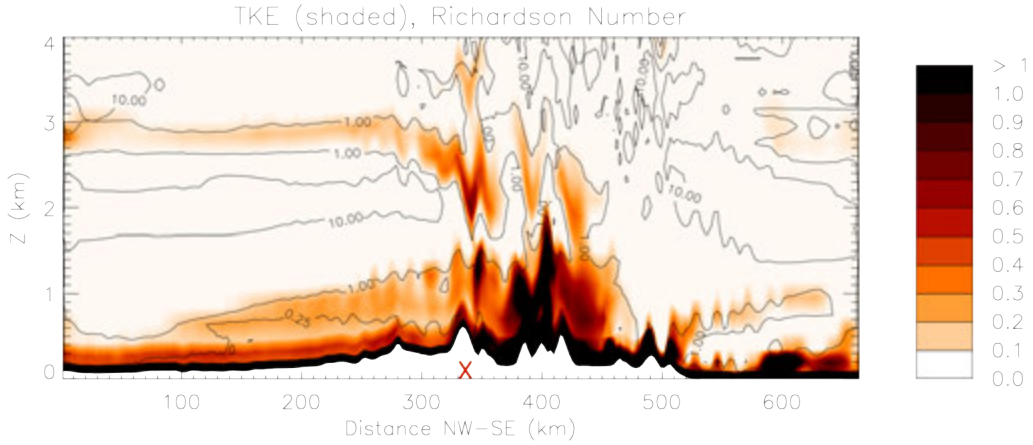

accident and in the eastern half of the figures the orientation, wavelength and amplitude of the waves compare well.

While the mountain waves produced in the small and large domain simulations are adequately resolved by the 1.85 km horizontal grid spacing, the sensitivity to this horizontal resolution is also considered here. Another simulation that uses the small domain, but twice the horizontal resolution (0.925 km horizontal grid spacing) is shown in Fig. 11(c). This higher resolution simulation shows that, despite differences in detail, the structure of the wave field is similar to the small domain 1.85 km grid spacing simulation. The higher resolution simulation contains waves with slightly smaller amplitude near the accident location. Yet, these differences are relatively minor, suggesting that (within reason) the results presented by the control simulation are not unduly affected by horizontal resolution.

Of course, with horizontal grid spacing of O (1 km), turbulence that affects aircraft is not properly resolved. Moreover, grid resolutions as small as tens of metres might be required to resolve the scales of motion that affect light aircraft. While it would be preferable to actually resolve the turbulence in a large-eddy simulation rather than rely on the sub-grid parameterisation to diagnose it, large-eddy simulations are beyond the resources available for this study. For this reason, estimates of enhanced *TKE* from these model simulations must be sourced from parameterised processes. Nonetheless, Lane et al. (2006) showed that the regions of enhanced sub-grid scale mixing produced by this same model with 1 km horizontal grid spacing (in the lee of the Hawaiian Island, Kauai), coincided with those regions of resolved turbulence that occurred in a 167 m grid spacing simulation of the same event. That result suggests that the modelled *TKE* reported here provides sufficient guidance regarding the potential locations of enhanced turbulence, especially given that these regions of enhanced *TKE* are ultimately derived from larger scale processes (viz. mountain waves) that are relatively insensitive to model resolution.

Fig. 10. Cross section from northwest (left) to southeast (right) through the centre of the domain of (a) potential temperature contoured at 1 K intervals; (b) the 315° component of the horizontal velocity contoured at 2 m s⁻¹ intervals; and (c) vertical shear contoured at 2 m s⁻¹ km⁻¹ intervals. The cross indicates the accident location.

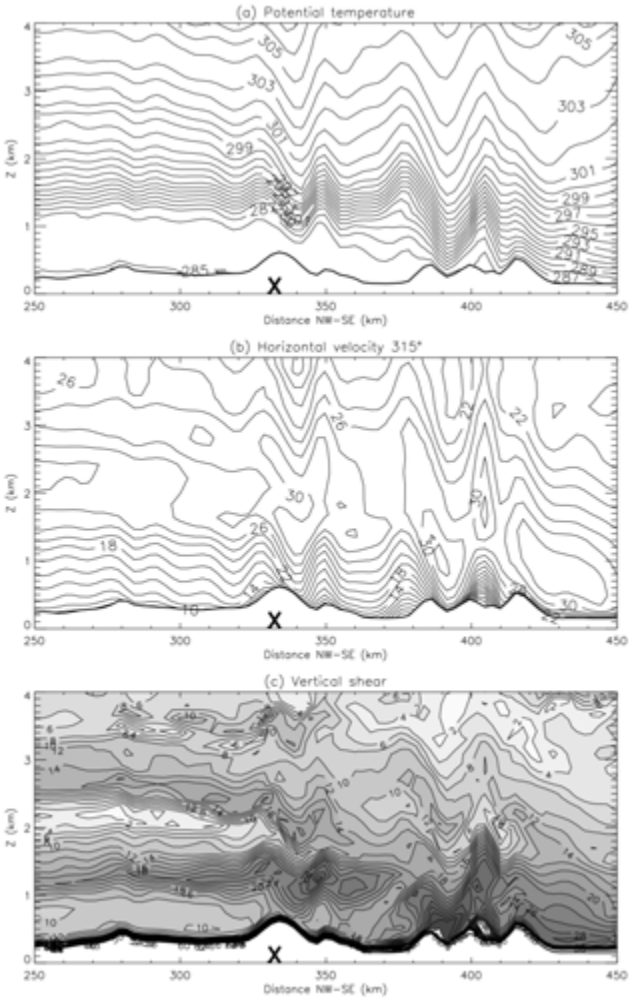

Fig. 11. Cross section at approximately 1.9 km AGL at six hours simulation time for the (a) large domain 1.85 km grid spacing simulation (control simulation), (b) the small domain 1.85 km grid spacing simulation, and (c) the small domain 0.925 km grid spacing simulation. Vertical velocity contoured at 0.5 m s^{-1} intervals, with negative values dashed. Topography contours are the same as Fig. 6(a).

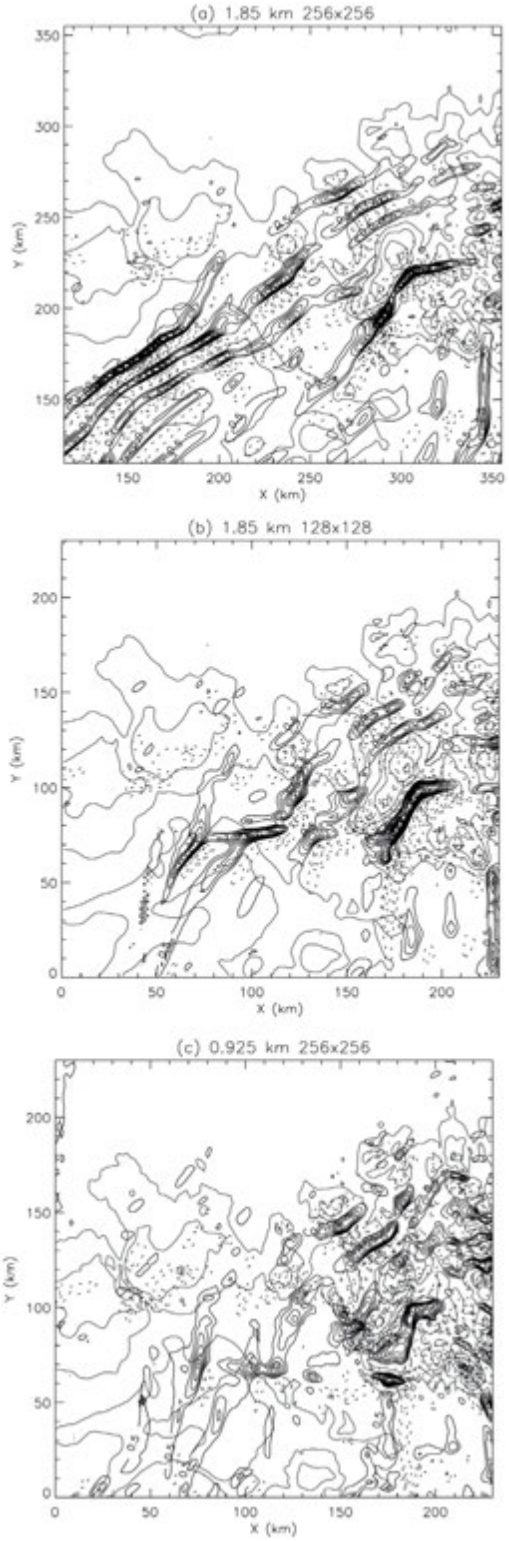

(f) A simple ensemble of simulations

As shown in (b) above, modifications to the upstream wind conditions were necessary to compensate for the enhancement in the low-level wind in the lee of the terrain and obtain agreement between the modelled and observed wind profiles. Yet, as shown in Fig. 1(b), some differences between the modelled and observed winds remain. In particular, the wind upstream of the terrain has a slight westerly bias and near Melbourne the bias is easterly. These errors place some additional uncertainty on the outcomes of the 3D simulations. Moreover, it is well known that turbulence has low predictability because of its small-scale and transient nature and because its generation is usually reliant on certain thresholds being crossed. This low predictability suggests that ensemble simulations of turbulent flow are more appropriate than single realisations. With these issues in mind, a simple ensemble of 3D simulations is constructed to explore the sensitivity of the simulated *TKE* to small variations in the upstream conditions. A set of simulations with perturbed upstream low-level wind directions is used. This ensemble not only provides a simple method to assess the uncertainty caused by modifications in the upstream wind profile, but also provides a demonstration of the potential value of ensemble methods for turbulence predictions.

A set of eleven simulations form the ensemble: in addition to the control simulation, ten simulations are performed using the large domain with different background wind profiles. Each profile is constructed by perturbing the wind direction below 5.2 km in the initial sounding by a constant value of –15°, –12.5°, –10°, –5°, –2.5°, 2.5°, 5°, 10°, 12.5°, and 15° (between 5.2 km and 6 km the strength of the perturbation is gradually reduced to zero). While not meant to be a statistically rigorous method of ensemble generation, this set of perturbations has a standard deviation of approximately 10°, 60 per cent of the directions fall within one standard deviation of the mean, and all fall within two standard deviations of the mean. Despite the simplicity, this ensemble set is sufficient to explore the sensitivity of the simulated lee waves and *TKE* to small variations in upstream wind direction.

Each of the eleven 3D ensemble members are analysed collectively at six hours when they are approximately at steady state to determine the spatial distribution of ensemble mean *TKE* and the *TKE* standard deviation (ensemble spread) at approximately 1.9 km AGL, which are shown in Figs 12(a) and 12(b). Figure 12(a) shows the ensemble mean to be largest in a west–east oriented band that extends approximately 50 km either side of the accident site, with values between 0.3–0.5 m^2 s^{-2}. However, the sensitivity of the parameterised turbulence to upstream wind direction is illustrated by an ensemble spread that is maximised in this band with the largest values between 0.2–0.4 m^2 s^{-2}, i.e. almost the same size as the mean. Nevertheless, above the accident site the ensemble spread possesses a local minimum, suggesting the enhanced turbulence in this region is a robust feature of the flow and insensitive to the upstream wind direction. Taking a

Fig. 12. (a) Ensemble mean *TKE* in $m^2 s^{-2}$; (b) ensemble spread *TKE* in $m^2 s^{-2}$; (c) the probability that $TKE \geq 0.1$ $m^2 s^{-2}$; and (d) the probability that *TKE* is ≥ 0.5 $m^2 s^{-2}$. All are shown at approximately 1.9 km AGL after six hours simulation time with topography contours the same as Fig. 6(a).

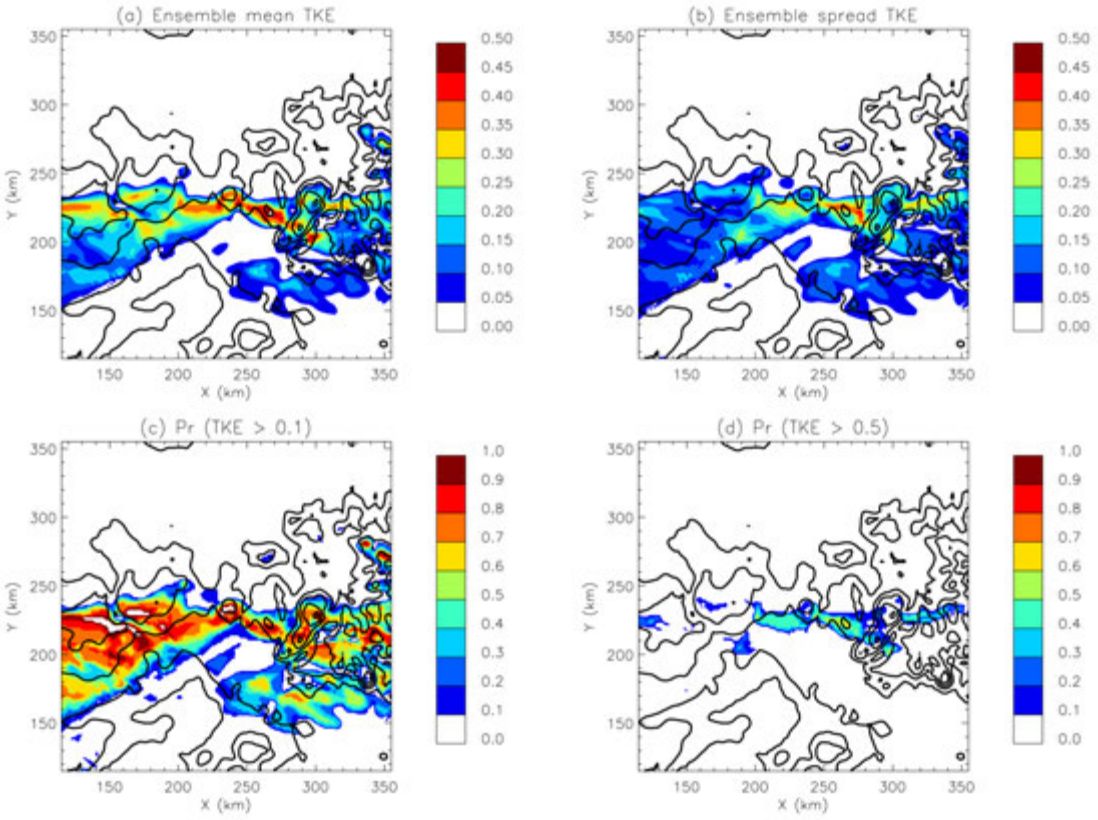

local area average of *TKE* in a 40 × 40 km box centred on the accident location for each ensemble member gives a range of *TKE* values of 0.021–0.226 $m^2 s^{-2}$; for the control simulation, the value is 0.157 $m^2 s^{-2}$. Ensemble members with positive perturbations to the wind profile present smaller local average *TKE* values than those with negative perturbations, with the control lying between the two groups.

The ensemble spread *TKE* (Fig. 12(b)) provides information about the uncertainty of the simulated *TKE* and demonstrates substantial sensitivity to upstream conditions above the mountain range, which could be caused by variability of turbulence occurrence, amplitude, or both. Further information about the *TKE* sensitivity can be obtained by examining exceedance probabilities. Specifically, for each horizontal grid point the number of ensemble members that exceed a certain *TKE* threshold is determined. When divided by the number of ensemble members (11 in this case), the resultant field can be interpreted as the probability that *TKE* exceeds the defined threshold at each location. Figures 12(c) and 12(d) show the probability that the *TKE* at approximately 1.9 km AGL exceeds 0.1 $m^2 s^{-2}$ and 0.5 $m^2 s^{-2}$, respectively. The smaller threshold (0.1 $m^2 s^{-2}$, Fig. 12(c)) demonstrates that there are many parts of the flow that contain non-zero *TKE* in almost all of the ensemble members (probability ≥ 0.9). Moreover, a small region directly above the accident site has non-zero *TKE* in all ensemble members, providing further evidence that the simulated *TKE* at this location is a robust feature of the flow. These large probabilities also imply that the ensemble spreads at these locations are associated with variability in *TKE* amplitude among the members, and not variability in *TKE* occurrence. This amplitude variability is further demonstrated by the reduction in probability of occurrence at the larger *TKE* threshold (Fig. 12(d)); in the vicinity of the accident site only ~40 per cent of the ensemble members exceed this threshold.

The relative lack of sensitivity of the simulated *TKE* to upstream wind direction is a result of the relative lack of sensitivity of the lee waves to those changes. Figure 13 presents vertical cross-sections of the vertical velocity for simulations with wind direction perturbations of –15°and 15°, i.e. the two largest perturbations from the control. Comparison between horizontal cross-sections of these vertical velocities (not shown) and Fig. 6 show local differences in wave orientation and some small differences in the location of the wave fronts, but no overall change in the flow regime. Moreover, in these perturbed cases the vertical structure of the lee waves near the accident site (Fig. 13(a,c)) are very similar to the control (Fig. 13(b)), again with some local differences in the location of the maximum vertical velocities. The wind direction changes do modify the cross-mountain wind speed (and hence Nh/u), but the resultant perturbations in cross-mountain wind speed are

Fig. 13. Cross-section from northwest (left) to southeast (right) of vertical velocity (shaded and contoured at 0.5 m s^{-1} intervals) and potential temperature from the ensemble members with (a) 15° and (c) –15° wind direction perturbations. The control simulation is shown in (b).

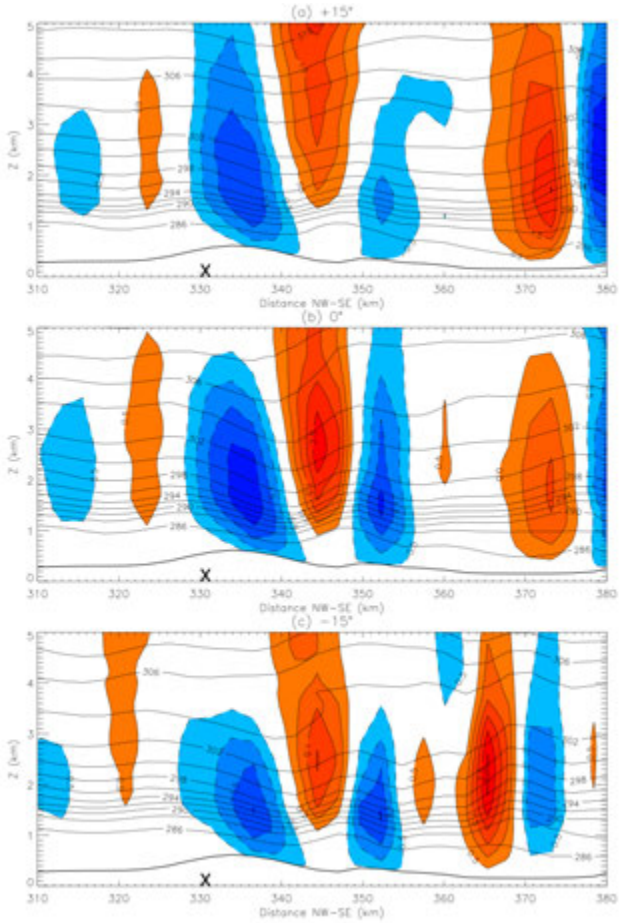

relatively small. These results are in agreement with those of Watson and Lane (2012) who showed that in a linear regime, i.e. Nh/u <<1, there is limited sensitivity of terrain-induced flows to upstream wind direction because small changes do not cause a regime transition. If the wind direction (or wind speed) perturbations are large enough to cause a significant change in Nh/u a regime shift is possible and the sensitivity is likely much larger.

Since the *TKE* is sourced from the model's sub-grid parameterisation, its values do not readily translate to a scale of turbulence severity for aviation. Instead, the *TKE* only provides a measure of the relative intensity of turbulence in different parts of the flow and the thresholds chosen in Figs 12(c,d) are somewhat arbitrary. Nonetheless, more sophisticated approaches can be used to estimate the severity of aircraft-scale turbulence from numerical models (e.g. Frehlich and Sharman 2004). Thus, if aircraft-scale turbulence intensities were determined for each member of an operational ensemble forecast, the method used to construct Figs 12(c,d) could provide probabilistic predictions of each level of turbulence severity (e.g. light, moderate, severe, etc.). Such an approach holds much promise for future operational predictions of turbulence.

Summary

On 31 July 2007 a fatal light aircraft crash occurred near Clonbinane, Victoria, Australia and the official investigation concluded that mountain wave turbulence was the likely cause. This study used a combination of idealised three-dimensional numerical modelling and linear wave theory to examine the dynamics of mountain waves during this turbulence event and their role in generating turbulence.

The linear analysis showed that the observed environment was conducive to trapped mountain waves and three-dimensional simulations showed trapped mountain waves above much of the elevated terrain. The waves possessed a variety of complicated trapped wave structures with different orientations. However, the predominant wave front orientation in the vicinity of the accident was perpendicular to the mean low-level wind shear, with the wave amplitudes maximised near the accident site. The three-dimensional simulation used horizontal grid spacing of 1.85 km, although additional simulations at higher resolution showed similar wave characteristics.

While the three-dimensional simulations were too coarse to properly resolve the scales of motion that influence small aircraft, the model's sub-grid parameterisation showed significant enhancements in parameterised turbulence in the vicinity of the accident. The trapped mountain waves were responsible for the enhanced turbulence by causing the ascent of a strong shear layer that originated near the surface, as well as the descent of a dynamically unstable layer that originated at approximately 3 km AGL. Both of these processes led to reduced Richardson number and localised maxima in parameterised turbulence near 2 km AGL, i.e. the aircraft's flight altitude, near the location of the accident.

A simple ensemble of three-dimensional simulations was also used to explore the sensitivity of the modelled turbulence to small variations in the upstream wind direction. These simulations showed that the occurrence of turbulence above the accident site was a robust feature of the simulations, lending further credence to the simulation results and the conclusion that mountain waves played an important role in generating the turbulence. The strength of the parameterised turbulence did, however, show some sensitivity to the changes in the upstream conditions. In addition to testing the robustness of the simulation results, the ensemble was used to demonstrate how high-resolution ensemble simulations could be readily interrogated to provide probabilistic turbulence information for forecasting applications. In that case, the predictive ensemble would also expose sensitivity to perturbations in variables other than wind directions and be more sophisticated than that presented here.

In summary, this study has examined the dynamics of

mountain waves and turbulence production during an event that led to a light aircraft accident. Despite the simplifications in the modelling approach, the balance of evidence suggests that turbulence caused or enhanced by trapped mountain waves could have been present over the accident site. Moreover, the modelling results have further demonstrated the utility of high-resolution (non-hydrostatic) numerical models in studying aircraft turbulence encounters, as well as their potential for explicit operational predictions of mountain wave turbulence. Such models have the potential to provide detailed guidance of the spatial distribution of turbulence and its intensity, neither of which are well characterised by existing warning methods (e.g. SIGMETs). As computational resources continue to increase, high-resolution forecasts and ensemble methods should provide significant improvements over existing approaches, providing invaluable guidance for turbulence hazard avoidance and route planning.

Acknowledgments

Todd Lane is the recipient of an Australian Research Council Future Fellowship (FT0990892). We thank Terry Clark for providing his numerical model, and Chermelle Engel and Andrea Henderson (Bureau of Meteorology) for providing operational forecast information and model data. This work was conducted while the lead author was an Honours student at the University of Melbourne. The authors thank the two anonymous reviewers for their input and improvements in the manuscript.

References

Australian Transport Safety Bureau (ATSB). 2009. ATSB Transport Safety Report – Occurrence Investigation Report AO-2007-029: Final. Available from: http://www.atsb.gov.au

Clark, T.L. 1977, A small-scale dynamic model using a terrain-following coordinate transformation. *J. Comput. Phys., 24,* 186–215.

Clark, T.L. and Hall, W.D. 1996. The design of smooth, conservative vertical grids for interactive grid nesting with stretching. *J. Appl. Meteorol., 35,* 1040–6.

Clark, T.L., Keller, T., Coen, J., Neilley, P., Hsu, H.-M. and Hall, W.D. 1997. Terrain-induced turbulence over Lantau Island: 7 June 1994 Tropical Storm Russ case study. *J. Atmos. Sci., 54,* 1795–814.

Clark, T.L., Hall, W.D., Kerr, R.M., Middleton, D. Radke, L., Ralph, M.R., Neiman, P.J. and Levinson, D. 2000. Origins of aircraft-damaging clear-air turbulence during the 9 December 1992 Colorado downslope windstorm: Numerical simulations and comparison with observations. *J. Atmos. Sci., 57,* 1105–31.

Deardorff, J.W. 1980. Stratocumulus-capped mixed layers derived from a three-dimensional model. *Bound.-Layer Meteor., 18,* 495–527.

Doyle, J.D. and Durran, D.R. 2002. The dynamics of mountain-wave induced rotors. *J. Atmos. Sci., 59,* 186–201.

Durran, D.R. 1986. Another look at downslope windstorms. Part I: The development of analogs to supercritical flow in an infinitely deep continuously stratified fluid. *J. Atmos. Sci., 43,* 2527–43.

Frehlich, R. and Sharman, R. 2004. Estimates of turbulence from numerical weather prediction model output with applications to turbulence diagnosis and data assimilation. *Mon. Weather Rev., 132,* 2308–24.

Jiang, Q. and Doyle, J.D. 2004. Gravity wave breaking over the central Alps: Role of complex terrain. *J. Atmos. Sci., 61,* 2249–66.

Jiang, Q., Doyle, J.D., Wang, S. and Smith, R.B. 2007. On boundary layer separation in the lee of mesoscale topography. *J. Atmos. Sci., 64,* 401–20.

Lane, T.P., Reeder, M.J., Morton, B.R. and Clark, T.L. 2000. Observations and numerical modelling of mountain waves over the Southern Alps of New Zealand. *Q. J. R. Meteorol. Soc., 126,* 2765–88.

Lane, T.P., Sharman, R.D., Clark, T.L. and Hsu, H.-M. 2003. An investigation of turbulence generation mechanisms above deep convection. *J. Atmos. Sci., 60,* 1297–321.

Lane, T.P., Sharman, R.D., Frehlich, R.G., and Brown, J.M. 2006. Numerical simulations of the wake of Kauai. *J. Appl. Meteor. Climatol., 45,* 1313–31.

Lane, T.P., Doyle, J.D., Sharman, R.D., Shapiro, M.A. and Watson, C.D. 2009. Statistics and dynamics of aircraft encounters of turbulence over Greenland. *Mon. Weather Rev., 137,* 2687–702.

Lane, T.P., Sharman, R.D., Trier, S.B., Fovell, R.G. and Williams, J.K. 2012. Recent advances in the understanding of near-cloud turbulence. *Bull. Am. Meteorol. Soc., 93,* 499–515.

Lilly, D.K. 1962. On the numerical simulation of buoyant convection. *Tellus, 14,* 145–72.

Lilly, D.K. 1978. A severe downslope windstorm and aircraft turbulence event induced by a mountain wave. *J. Atmos. Sci., 35,* 59–77.

Puri, K., Dietachmayer, G.S., Mills, G.A., Davidson, N.E., Bowen, R.A. and Logan, L.W. 1998. The new BMRC Limited Area Prediction System, LAPS. *Aust Meteorol. Mag., 47,* 203–23.

Scorer, R.S. 1949. Theory of waves in the lee of mountains. *Q. J. R. Meteorol. Soc., 75,* 41–56.

Sharman, R., Hall, W., Keller, T. and Wolff, J. 2004. The operational prediction of mountain wave turbulence using a high resolution nonhydrostatic mesoscale model. *Proc. 11th Conf. on Aviation, Range and Aerospace Meteorology,* Hyannis MA, 4–7 October. Paper 4.12.

Sharman, R., Tebaldi, C., Wiener, G. and Wolff, J. 2006. An integrated approach to mid- and upper-level turbulence forecasting. *Weath. Forecasting, 21,* 268–87.

Sharman, R.D., Trier, S.B., Lane, T.P. and Doyle, J.D. 2012. Sources and dynamics of turbulence in the upper troposphere and lower stratosphere: A review. *Geophys. Res. Lett., 39,* L12803, doi:10.1029/2012GL051996.

Smagorinsky, J. 1963. General circulation experiments with the primitive equations. Part I. The basic experiment. *Mon. Weather Rev., 91,* 99–164.

Smolarkiewicz, P.K. and Rotunno, R. 1989. Low Froude number flow past three-dimensional obstacles. Part I: Baroclinically generated lee vortices. *J. Atmos. Sci., 46,* 1154–64.

Uhlenbrock, N.L., Bedka, K.M., Feltz, W.F. and Ackerman, S.A. 2007. Mountain wave signatures in MODIS 6.7-μm imagery and their relation to pilot reports of turbulence. *Weath. Forecasting, 22,* 662–70.

Watson, C.D. and Lane, T.P. 2012. Sensitivities of orographic precipitation to terrain geometry and upstream conditions in idealized simulations. *J. Atmos. Sci., 69,* 1208–31.

Wolff, J.K. and Sharman, R.D. 2008. Climatology of upper-level turbulence over the contiguous United States. *J. Appl. Meteor. Climatol., 47,* 2198–214.